Materials Horizons

ROYAL SOCIETY OF CHEMISTRY

COMMUNICATION

View Article Online
View Journal | View Issue

Cite this: *Mater. Horiz.*, 2022, 9, 334

Received 3rd April 2021,
Accepted 1st July 2021

DOI: 10.1039/d1mh00552a

rsc.li/materials-horizons

A computational scheme for evaluating the phosphorescence quantum efficiency: applied to blue-emitting tetradentate Pt(II) complexes†

Yu Wang,[a] Qian Peng [b] and Zhigang Shuai *[a]

Phosphorescent organic light-emitting diodes (PhOLEDs) are leading candidates for displays or lighting technologies. Recently, blue phosphorescent tetradentate Pt(II) complexes have been attracting extensive attention due to their high phosphorescence quantum efficiency and numerous chemical structures on account of flexible ligand frames and modifications. Using quantum chemistry coupled with our thermal vibration correlation function (TVCF) formalism, we investigated the triplet excited state energy surface and the decay processes involving both direct vibrational relaxation and minimum energy crossing point (MECP) *via* the transition state (^{3}TS) to the ground state (S_0) for 16 recently experimentally reported blue-emitting tetradentate Pt(II) emitters containing fused 5/6/6 metallocycles. We found that (i) in most cases, the direct vibrational relaxation deactivations dominated the triplet non-radiative decay because either the ^{3}TS is too high or the MECP is not reachable. Hence, results from the TVCF formalism agreed well with the experiments for the phosphorescence quantum efficiency; (ii) only when both ^{3}TS and MECP are low, for instance, for PtON1-oMe, deactivations *via* MECP dominated the triplet non-radiative decay.

New concepts

Organometallic complexes have been widely applied in phosphorescent organic light-emitting diodes (PhOLEDs). It is essential to quantitatively predict phosphorescence quantum efficiencies for these light-emitting materials from a theoretical aspect. In this study, we quantitatively calculated all possible triplet decay rates for a series of newly developed blue-emitting tetradentate Pt(II) complexes under the framework of thermal vibration correlation function (TVCF) and transition state theory (TST). For blue-emitting organometallic complexes, it was generally believed that the metal-centered (MC) state is the leading deactivation channel. We found for the first time that commonly for newly developed Pt-complexes, deactivation channel *via* MC is usually prohibited due to either the transition state ^{3}TS is too high or the minimum energy crossing point (MECP) is unreachable. Therefore, the TVCF framework can serve as an efficient and accurate tool in evaluating phosphorescence quantum efficiencies for blue-emitting tetradentate Pt complexes.

Introduction

Phosphorescent organic light-emitting diodes (PhOLEDs) are the most employed components in the organic electronics industry.[1–3] Phosphorescent emitters, including cyclometalated Ir(III) and Pt(II) complexes, have attracted considerable attention due to the 100% electroluminescence internal quantum efficiency (IQE) caused by strong spin–orbit coupling effects that could efficiently harness both singlet and triplet excitons.[4–6] However, the development of highly efficient deep-blue organometallic emitters is still of significant challenge, mainly due to their attainable metal-centered d–d quenching states.[7,8] Recently, a rapid progress has been made in the development of efficient deep-blue OLEDs employing Pt(II) complexes that have met or even exceeded the performance of Ir(III) complexes in many aspects.[9,10] On the one hand, Pt(II) complexes have demonstrated phosphorescence quantum efficiencies (Φ_p) close to unity and a short luminescence lifetime in the range of microseconds at room temperature, thus making them advantageous as phosphorescent emitters.[11] On the other hand, square planar Pt(II) complexes have multiple chemical structures that could be assigned with various frames of ligands, including bidentate, tridentate, and tetradentate ligand scaffolds.[12–14] Typically, Pt(II) complexes with bidentate or tridentate ligands suffer from low quantum efficiencies or poor stabilities owing to their readily distorted geometries or monoanionic ligands.[15,16] In contrast, Pt(II) complexes with a tetradentate ligand frame, which afford rigid structural scaffolds, exhibit high Φ_p as well as good thermal and electrochemical stabilities.[17] Given the diverse metallocycle arrangements, several types of tetradentate

---

[a] *MOE Key Laboratory of Organic OptoElectronics and Molecular Engineering, Department of Chemistry, Tsinghua University, Beijing 100084, P. R. China. E-mail: zgshuai@tsinghua.edu.cn*

[b] *School of Chemical Sciences, University of Chinese Academy of Sciences, Beijing 100049, P. R. China*

† Electronic supplementary information (ESI) available. See DOI: 10.1039/d1mh00552a

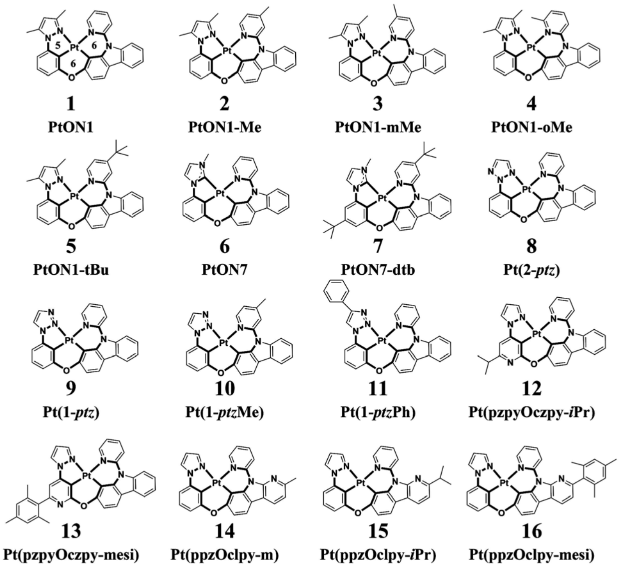

Scheme 1 Structures of 16 blue-emitting tetradentate Pt(II) emitters containing fused 5/6/6 metallocycles. (**2-ptz** = 2-phenyl-1,2,3-triazole; **1-ptz** = 1-phenyl-1,2,3-triazole; **ppz** = phenyl-pyrazol; **pzpy** = pyrazol-pyridine; **czpy** = pyridyl-carbazole; **clpy** = pyridyl-carboline; **iPr** = iso propyl; **mesi** = mesityl)

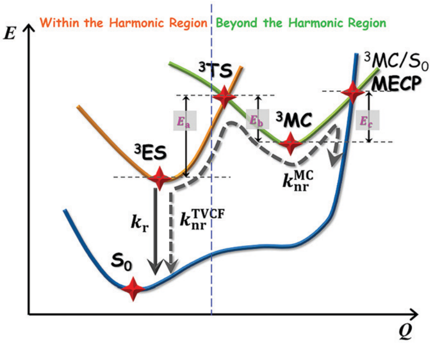

Scheme 2 Schematic representation of the competing excited-state deactivations of Pt(II) complexes. k_r and $k_{nr}{}^{TVCF}$ are the radiative and non-radiative decay rates from the triplet emissive state (^{3}ES) to the ground state (S$_0$) within the harmonic region, and $k_{nr}{}^{MC}$ is the thermally activated nonradiative decay rate beyond the harmonic region. E_a, E_b, and E_c are the electronic energy barriers among ^{3}ES, ^{3}TS, ^{3}MC, and MECP states (^{3}TS represents the transition state between ^{3}ES and ^{3}MC states, and MECP is the S$_0$/^{3}MC minimum energy crossing point).

Pt(II) complexes have been developed by now. It is noteworthy to mention that tetradentate Pt(II) complexes with 5/6/5 or 5/5/6 fused metallocycles exhibit planar molecular geometries and are apt to form excimer emissions, enabling them to act as ideal emitters for single-doped white OLEDs.[18] Correspondingly, tetradentate Pt(II) complexes with 5/6/6 or 6/6/6 fused metallocycles are more twisty in structure that prevent intermolecular interactions, thereby making them suitable for monochromic luminescence.[19,20] In this study, sixteen blue-emitting tetradentate Pt(II) emitters containing fused 5/6/6 metallocycles that have been synthesized and characterized in experiments were chosen for theoretical investigations, as shown in Scheme 1.[21–24] These tetradentate Pt(II) emitters are similar in structure yet different in monomeric photophysical properties.

The photophysical model adopted in this study is depicted in Scheme 2. The electro-pumped carriers form the lowest triplet excited state, which would undergo several processes. The radiative decay rate for a two-level system could be evaluated by the Einstein spontaneous emission rate as $k_r = \frac{8\pi^2 v_{fi}^3}{3\varepsilon_0 \hbar c^3}\mu_{fi}^2 \approx \frac{f v_{fi}^2}{1.5}$, which ranges $\sim 10^{2-6}$ s^{-1} for phosphorescent with μ_{fi} (f), the cross spin–manifold transition electric dipole moment (oscillator strength) between the initial and final states to give rise to photon with transition energy ν_{fi} in wavenumber. When vibrational levels were considered, a more elaborated formula was given by eqn (1). Within the harmonic oscillator approximation, the non-radiative decay rates ($k_{nr}{}^{TVCF}$) from the triplet emissive state (^{3}ES) to the ground state (S$_0$) can be evaluated *via* the thermal vibration correlation function (TVCF) rate theory, which was earlier developed by us, in combination with the quantum chemistry calculations for relevant molecular parameters. This theory has been demonstrated to be precise and efficient in numerous cases if the potential energy surface crossing effects can be ignored.[25–28] For organometallic compounds, the metal-centered (^{3}MC) states could play an essential role in triplet deactivations. Among the complexes considered in this study, the most significant geometry change in the processes of ^{3}ES → ^{3}MC → MECP is the variations in the dihedral angle N1–C1–N2–C2, and soft scans of the lowest triplet excited states over this dihedral angle in complex **1** are depicted in Fig. S1 (ESI†), which illustrates that the non-radiative decay including ^{3}MC is beyond the harmonic region. In such cases, the additional non-radiative decay rate $k_{nr}{}^{MC}$ (beyond the harmonic region) should be considered and be quantitatively evaluated *via* a kinetic model, involving equilibration between ^{3}ES and ^{3}MC states before irreversible return to the S$_0$ state.[29,30] More details can be found under the "Methods" section. The calculated phosphorescence quantum efficiencies without and with considerations of $k_{nr}{}^{MC}$ are expressed as $\Phi_p{}^{TVCF} = k_r/(k_r + k_{nr}{}^{TVCF})$ and $\Phi_p{}^{MC} = k_r/(k_r + k_{nr}{}^{TVCF} + k_{nr}{}^{MC})$, respectively. This study will show that only one complex, **PtON1-oMe**, possesses both low ^{3}TS (transition states between ^{3}ES and ^{3}MC) and MECP, contributing considerably to the triplet deactivations. In principle, $\Phi_p{}^{MC}$ is more general than $\Phi_p{}^{TVCF}$, but MC is much more complicated to evaluate. For the rest of the blue-emitting tetradentate Pt(II) complexes, phosphorescence efficiencies calculated *via* the TVCF framework ($\Phi_p{}^{TVCF}$) are comparable with experimental measurements owing to their unreachable ^{3}TS or MECP.

Methods

The vibrational relaxation decay rates of k_r and $k_{nr}{}^{TVCF}$ are calculated *via* a home-built MOMAP program.[31] k_r can be obtained by the integration over the whole range of the emission spectrum:[32]

$$k_r = \int \sigma_{em}(\omega, T)\mathrm{d}\omega \tag{1}$$

where

$$\sigma_{\mathrm{em}}(\omega, T) = \frac{4\omega^3}{3\hbar c^3} \sum_{v_{\mathrm{i}} v_{\mathrm{f}}} P_{iv_{\mathrm{i}}}(T) \left| \langle \theta_{\mathrm{f},v_{\mathrm{f}}} | \mu_{\mathrm{fi}} | \theta_{i,v_{\mathrm{i}}} \rangle \right|^2 \delta(\omega_{iv_{\mathrm{i}} f v_{\mathrm{f}}} - \omega) \quad (2)$$

$\mu_{\mathrm{fi}} = \langle \Phi_{\mathrm{f}} | \vec{\mu} | \Phi_{\mathrm{f}} \rangle$ is the electric transition dipole moment between the final and initial electronic states; $P_{\mathrm{iv_i}}$ is the Boltzmann distribution function for the initial state vibration manifold; Φ and θ are the electronic and vibrational wavefunctions, respectively. Under the Franck–Condon approximation, the emission spectra $\sigma_{\mathrm{e,m}}(\omega,T)$ in TVCF formalism can be expressed as:

$$\sigma_{\mathrm{em}}^{\mathrm{FC}}(\omega, T) = \frac{2\omega^3}{3\pi\hbar c^3} |\mu_{\mathrm{fi}}|^2 \int_{-\infty}^{\infty} e^{-i(\omega - \omega_{\mathrm{if}})t} \rho_{\mathrm{em},0}^{\mathrm{FC}}(t, T) \mathrm{d}t \quad (3)$$

where $\rho_{\mathrm{em},0}{}^{\mathrm{FC}}(t,T)$ is the TVCFs and can be formulated as $Z_{\mathrm{i}}^{-1} Tr\left[e^{-i\tau_{\mathrm{f}}\hat{H}_{\mathrm{f}}} e^{-i\tau_{\mathrm{i}}\hat{H}_{\mathrm{i}}}\right]$, which can be analytically solved by multi-dimensional Gaussian integrations; $\tau_{\mathrm{i}} = -i\beta - t/\hbar$; $\tau_{\mathrm{f}} = t/\hbar$; $\beta = (k_{\mathrm{B}}T)^{-1}$ and $\hat{H}_{\mathrm{f}}$ ($\hat{H}_{\mathrm{i}}$) is the harmonic oscillator Hamiltonian of the final (initial) electronic states. As for $k_{\mathrm{nr}}{}^{\mathrm{TVCF}}$, which is the non-radiative decay rate within the harmonic region, can be expressed as:[26]

$$k_{\mathrm{nr}}{}^{\mathrm{TVCF}} \equiv \frac{1}{\hbar^2} \left| H_{\mathrm{fi}}^{\mathrm{SO}} \right|^2 \int_{-\infty}^{\infty} e^{i\omega_{\mathrm{if}} t} \rho_{\mathrm{fi}}^{(0)}(t) \mathrm{d}t \quad (4)$$

where $H_{\mathrm{fi}}{}^{\mathrm{SO}} = \langle \Phi_{\mathrm{f}} | \hat{H}_{\mathrm{SOC}} | \Phi_{\mathrm{i}} \rangle$ is the spin–orbit coupling matrix between two electronic states; $\rho_{\mathrm{fi}}^{(0)}(t)$ is the same with $\rho_{\mathrm{em},0}^{\mathrm{FC}}(t,T)$.

For the calculation of $k_{\mathrm{nr}}{}^{\mathrm{MC}}$ that is beyond the harmonic region, a kinetic model, which assumes equilibrium between the ^{3}ES and ^{3}MC states before irreversible return to the ground state, is employed as $^3\mathrm{ES} \underset{k_{\mathrm{b}}}{\overset{k_{\mathrm{a}}}{\rightleftharpoons}} {}^3\mathrm{MC} \xrightarrow{k_{\mathrm{c}}} \mathrm{S}_0$. Using the steady-state approximation, the $k_{\mathrm{nr}}^{\mathrm{MC}}$ can be expressed as

$$k_{\mathrm{nr}}^{\mathrm{MC}} = \frac{k_{\mathrm{c}} k_{\mathrm{a}}}{k_{\mathrm{c}} + k_{\mathrm{b}}} = A_0 k_{\mathrm{a}} \quad (5)$$

where $A_0 = 1 \Big/ \left[1 + \exp\left(\frac{E_{\mathrm{c}} - E_{\mathrm{b}}}{k_{\mathrm{B}} T}\right)\right]$ (E_{b} and E_{c} being the electronic energy barriers, as shown in Scheme 2) and k_{a} can be evaluated *via* the transition state theory (TST) Eyring equation as:[33]

$$k_{\mathrm{a}} = \frac{k_{\mathrm{B}} T}{h} \exp\left(-\frac{\Delta G_{\mathrm{a}}^{\neq}}{RT}\right) \quad (6)$$

where $\Delta G_{\mathrm{a}}{}^{\neq}$ is the Gibbs free energy of activation between ^{3}ES and ^{3}TS states, which was evaluated using the Shermo program;[34] k_B is the Boltzmann's constant, h is the Planck's constant, and T is the temperature (T = 298 K).

As appeared in the above formula eqn ((1)–(6)), there contained numerous molecular parameters, including electronic structures and vibrational modes as well as their couplings. These were evaluated with the density functional theory (DFT) and time-dependent DFT (TDDFT), as implemented in the *Gaussian16* software.[35] Geometry optimizations were performed for the S$_0$, ^{3}ES, ^{3}TS, and ^{3}MC states, as well as the S$_0$/^{3}MC minimum energy crossing point (MECP) with the hybrid Perdew–Burke–Ernzerhof (PBE0)[36] functional in combination with the third version of Grimme's atom pair-wise dispersion corrections with Becke–Johnson damping (D3BJ).[37,38] The ^{3}MC states are searched by rotating the aromatic rings containing the N–Pt coordination bond in the tetradentate ligand scaffold on account of strong electronic repulsion between the metal and nitrogen atom when the electronic excitation is of metal-centered character. The MECPs were optimized by the sobMECP program.[39] All structural optimizations were carried out using a polarizable continuum model (PCM) taking solvent effects into account.[40] The unrestricted formalism was used for the geometry optimizations of triplet states. Vibrational frequency calculations at the same level of the theory for geometry were conducted to affirm the nature of the stationary points of geometries. For S$_0$, ^{3}ES and ^{3}MC minimum states, there was no imaginary frequency, while for ^{3}TS states, there exists one mode with an imaginary frequency. The basis set combining with Stuttgart Dresden ECP (SDD)[41] is chosen for heavy atom Pt(II), and the 6-31G** basis set is adopted for light atoms. Four kinds of functionals, namely PBE0, M06,[42] M062X,[42] and PBE38,[37] were employed for triplet-emitting spectral calculations, and PBE38 was chosen as the most suitable one. All single-point calculations were calculated *via* PBE38 functional, with the same basis sets as optimizations. Spin–orbit coupling (SOC) of singlet and triplet states calculations are carried out with the PySOC package.[43] The Dalton program[44,45] was employed for the calculations of the ^{3}ES → S$_0$ transition dipole moment μ_{fi} at the B3LYP[46,47]/6-31g**/SDD theoretical level. The hole–electron distribution analysis for ^{3}ES → S$_0$ excitations was conducted by the Multiwfn program.[48,49]

Results and discussion

Triplet excitation properties

First, geometries of S$_0$ and ^{3}ES states for these 16 tetradentate Pt(II) complexes are optimized *via* PBE0 functional, which has been demonstrated accurately for Pt(II) complex optimizations in numerous documents.[15,16,50] Next, triplet emission properties were evaluated with four different functionals. The triplet emission peaks in solutions of experimental and theoretical results are given in Table 1. It can be seen that PBE38 functional has the least mean absolute error (MAE), which was chosen for the triplet emission property calculations.

The tetradentate ligand is divided into three parts, as shown in Fig. 1a, for the sake of analysis. Fig. 1b presents the calculated hole–electron distributions of ^{3}ES → S$_0$ excitations for Pt(II) complexes, where red represents the hole distribution and green represents the electron distribution. Transition characters of ^{3}ES → S$_0$ processes for these Pt(II) complexes are dominated by the triplet ligand to ligand charge transfer (^{3}LLCT) or intraligand (^{3}IL), mixed with metal to ligand charge transfer (^{3}MLCT), as listed in Table 2. Comparing complexes **1–5**, the introduction of an electron-donating group such as methyl or tertiary butyl on the para position of pyridine (just as **2** and **5**) decreases charge distributions on the **L1** part efficiently, whereas the introduction of a methyl group on the meta or ortho position of pyridine has no such effect. Note that

Table 1 Experimental and computational results of triplet emission peaks for 16 chosen Pt(II) complexes in solutions at their optimized ^{3}ES geometries

	λ_{em}[a] (nm,exp)	λ_{em}[a] (eV,exp)	λ_{em} (eV,PBE38)	λ_{em} (eV,PBE0)	λ_{em} (eV,m06)	λ_{em} (eV,m062x)
1	478	2.5941	2.8404	2.4999	2.4919	3.1629
2	444	2.7928	2.6619	2.5875	2.5599	2.9569
3	476	2.6050	2.8471	2.5226	2.5089	3.1435
4	450	2.7556	2.9021	2.5990	2.5935	3.1989
5	444	2.7928	2.6644	2.5892	2.5601	2.9586
6	452	2.7434	2.8619	2.5300	2.5245	3.1861
7	446	2.7803	2.9303	2.5994	2.5926	3.2549
8	464	2.6724	2.7297	2.4607	2.4242	3.0889
9	468	2.6496	2.6723	2.4047	2.3648	3.0170
10	476	2.6050	2.6694	2.4008	2.3603	3.0135
11	480	2.5833	2.6206	2.3677	2.3287	2.9481
12	456	2.7193	2.6959	2.5326	2.4977	2.9637
13	458	2.7074	2.6659	2.5111	2.4753	2.9412
14	466	2.6609	2.4738	2.4228	2.3950	2.7571
15	464	2.6724	2.4747	2.4240	2.3943	2.7548
16	481	2.5780	2.3644	2.3083	2.2779	2.6343
MAE			0.1279	0.1993	0.2255	0.3051

[a] Experimental results of **1–7** are from ref. 21 in CH_2Cl_2, of **8–11** are from ref. 22 in 2-MeTHF, of **12** and **13** are from ref. 23 in CH_2Cl_2, of **14–16** are from ref. 24 in CH_2Cl_2, respectively.

Table 2 The electron–hole difference of atom Pt, **L1**, **L2**, and **L3** parts of Pt(II) complexes as well as transition characters of ^{3}ES → S_0 processes. ($^3L_2L_1$CT means charge transfer from **L2** to **L1**; $^3IL_2$ means intraligand character centered on the **L2** part)

	ΔPt %	ΔL1 %	ΔL2 %	ΔL3 %	Character
1	−13.32	57.85	−39.48	0.28	$^3L_2L_1CT/^3MLCT$
2	−2.31	5.61	1.06	−0.15	$^3IL_2/^3MLCT$
3	−12.57	56.26	−40.54	1.03	$^3L_2L_1CT/^3MLCT$
4	−10.89	43.77	−30.18	1.81	$^3L_2L_1CT/^3MLCT$
5	−2.61	5.81	1.07	−0.10	$^3IL_2/^3MLCT$
6	−10.87	49.73	−30.89	−1.32	$^3L_2L_1CT/^3MLCT$
7	−12.97	45.79	−22.03	−4.01	$^3L_2L_1CT/^3MLCT$
8	−7.81	1.31	−22.91	40.56	$^3L_2L_3CT/^3MLCT$
9	−12.48	0.79	−24.67	46.43	$^3L_2L_3CT/^3MLCT$
10	−12.52	0.03	−24.20	46.80	$^3L_2L_3CT/^3MLCT$
11	−14.75	0.34	−20.64	43.40	$^3L_2L_3CT/^3MLCT$
12	−14.33	−0.09	−3.11	21.62	$^3IL_3/^3MLCT$
13	−12.97	0.13	−2.72	19.90	$^3IL_3/^3MLCT$
14	−2.03	1.67	5.34	−1.31	$^3IL_2/^3MLCT$
15	−1.85	1.43	5.43	−1.40	$^3IL_2/^3MLCT$
16	−1.78	1.56	5.01	−1.61	$^3IL_2/^3MLCT$

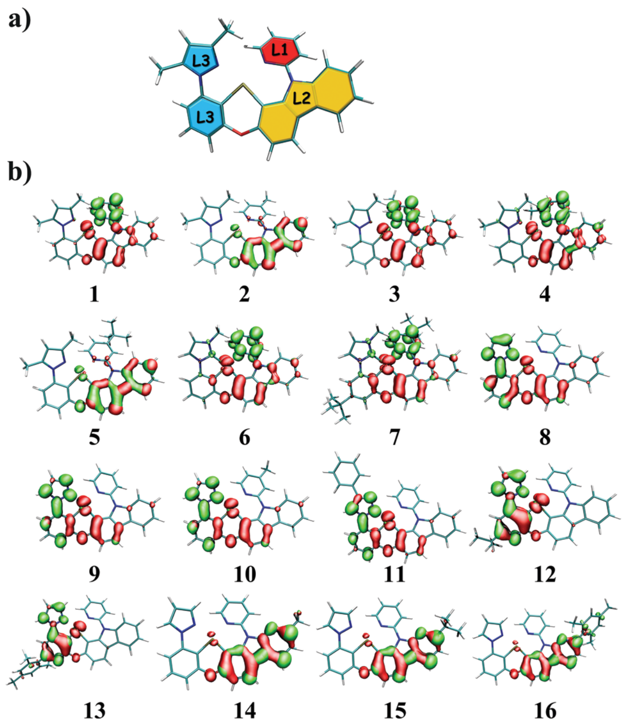

Fig. 1 (a) The tetradentate ligand was divided into three parts, namely **L1** (red), **L2** (yellow), and **L3** (blue); (b) distributions of hole and electron of ^{3}ES → S_0 excitations for Pt(II) complexes in this study (isovalue = 0.002), where red represents the hole distribution and green represents the electron distribution.

introducing tertiary butyl on the para position of pyridine within complex **7**, whereby the **L3** part (imidazole carbene) is different from that (pyrazole) in complexes **1–5**, cannot decrease electron distributions on the **L1** part. The ^{3}ES → S_0 excitations listed in Table S1 (ESI†) show that coefficients in the configuration interaction expansions are higher than 10% for seven representative complexes. Comparing **2** and **7**, it was found that both of them have an electron-donating group substituted on the para position of pyridine in the **L1** part, although their spatial distributions of the highest occupied molecular orbital (HOMO) are similar, while their spatial distributions of the lowest unoccupied molecular orbital (LUMO) are quite different, as depicted in Fig. S2 (ESI†). For complex **2**, the LUMO was diffused over the whole molecule, while for **7**, it was more localized on the **L1** partowing to the stronger electron-donating capability of imidazole carbene in complex **7** that prevented charge diffusions.

When the pyrazole moiety in the **L3** part was replaced with triazole, like complexes **8–11**, the electron distribution was mainly concentrated on the **L3** part. Comparing complexes **1** and **8**, it was found that both of them were dominated by H → L transition in ^{3}ES → S_0 excitations, as shown in Table S1 (ESI†). However, on account of the stronger electron-withdrawing ability of triazole in complex **8**, the spatial distribution of LUMO in **8** spread mainly over the **L3** part, while the LUMO of **1** was primarily localized on the **L1** part, as shown in Fig. S2 (ESI†).

For complexes **12** and **13**, in which the phenyl moiety in the **L3** part was replaced with pyridine, the electron distributions were also mainly localized on the **L3** part. Since pyridine is more electron-withdrawing than phenyl, the LUMO of **12** is mainly distributed on the **L3** part, as presented in Fig. S2 (ESI†). When the carbazole group in the **L2** part was replaced by the carboline moiety, which is less electron-donating, the transitions of ^{3}ES → S_0 are typically concentrated on the **L2** part, as exhibited in complexes **14–16**.

Radiative and non-radiative decay within the harmonic region

The calculated k_r and k_{nr}^{TVCF} *via* the TVCF framework are listed in Table 3. Critical parameters relating to k_r and k_{nr}^{TVCF}, including ^{3}ES → S_0 adiabatic energy difference (ΔE_{ad}), transition dipole moment ($\mu_{\text{tran.}}$), spin–orbit coupling (SOC) and reorganization energies (Reorg.), are also laid out in Table 3. It can be seen that the calculated radiative decay rates k_r (cal.) have the same order of magnitude of experimental results k_r (exp.), which is in the range of 10^4 s^{-1}–10^5 s^{-1}, indicating the reliability of the TVCF method, which is the first principle without any empirical parameters.

To investigate the processes of non-radiative decay within the harmonic region, the reorganization energies of $^3ES \rightarrow S_0$ are further decomposed into internal coordinates, namely bond lengths, bond angles and dihedral angles. The internal coordinates with the first five highest contributions to the total reorganization energies are depicted in Fig. S3 (ESI†). It is interesting to note that the area of these internal coordinate vibrations exactly corresponds to the electron distribution of each complex, as shown in Fig. 1b. For example, the electron distributions are focused on the **L1** part in complex **1**, so that its bond length stretching vibrations contributing the most to total reorganization energies were also located on the **L1** region. There has been a general correlation between the absolute amount of charge transfer on metal Pt atom in $^3ES \rightarrow S_0$ processes (|ΔPt| %) and SOC values, except for complexes **12** and **13**, as shown in Fig. 2. Comparing **10–13**, although they have nearly the same |ΔPt| %, the SOC of **10** and **11** is more than two orders of magnitude larger than that of **12** and **13.** It is because the excitation coefficients of H → L in **10** and **11** (∼0.8) are higher than that in **12** and **13** (∼0.6) in $^3ES \rightarrow S_0$ processes (see Table S2, ESI†), as SOC integrals are proportional to the excitation coefficients and coefficients of AO basis.[51] Note that when the carbazole group in the **L2** part was replaced by the carboline moiety as in **14–16**, |ΔPt| % decreased the most, thus leading to small SOC. The reorganization energies of $^3ES \rightarrow S_0$ for these 16 blue-emitting tetradentate Pt(II) complexes were less than 0.4 eV, and together with SOC ranging from 49 cm^{-1} to 215 cm^{-1}, their non-radiative decay rates of $^3ES \rightarrow S_0$ within the harmonic region were less than 10^5 s^{-1} ($k_{nr}^{TVCF} < 10^5$ s^{-1}).

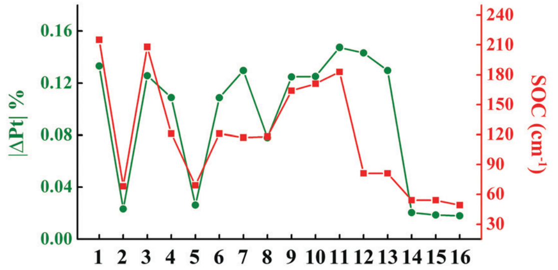

Fig. 2 Line graphs of calculated the absolute amount of charge transfer in $^3ES \rightarrow S_0$ processes on Pt atom (|ΔPt| %) and SOC values for 16 Pt(II) complexes.

Non-radiative decay beyond the harmonic region

As is known, the transfer of thermal population to the ^3MC state state from the ^3ES is an effective pathway for the non-radiative decay of organometallic complexes, so that the accessibility of the ^3MC state can always be expected to have significant impacts on triplet deactivation processes. Herein, ^3MC states for all 16 tetradentate Pt(II) complexes were optimized at first, and then ^3TS states between ^3ES and ^3MC states were confirmed. For these 16 Pt(II) complexes, stable ^3MC states could be found when rotating the pyridine ring in the **L1** part, and the spin density of ^3MC states is presented in Fig. S4 (ESI†). As the complexes investigated in this study were highly unsymmetric, more than one MC state should be considered.[52] Therefore, for representative complexes **1** and **8–12**, stable $^3MC'$ states of the rotating triazole ring in the **L3** part were also found and are shown in Fig. S5 (ESI†). The structures of ^3TS states were confirmed by the vibrational displacements of only one imaginary frequency, as depicted in Fig. S6 (ESI†).

Table 3 Calculated adiabatic energy difference between ^3ES and S_0 states (ΔE_{ad}), transition dipole of $^3ES \rightarrow S_0$ processes ($\mu_{\text{tran.}}$), spin–orbit coupling between ^3ES and S_0 states (SOC), reorganization energies of $^3ES \rightarrow S_0$ processes (Reorg.), k_r (cal.) and k_{nr}^{TVCF} (cal.) of $^3ES \rightarrow S_0$ processes within the harmonic region, as well as experimental results of k_r (exp.)

	ΔE_{ad} (eV)	$\mu_{\text{tran.}}$ (Debye)	SOC (cm^{-1})	Reorg. (cm^{-1})	k_r (s^{-1}, cal.)	k_{nr}^{TVCF} (s^{-1}, cal.)	k_r^a (s^{-1}, exp.)
1	3.21	0.30	215	2144	3.16×10^5	3.19×10^3	2.15×10^5
2	2.99	0.20	68	2047	1.06×10^5	1.10×10^4	8.90×10^4
3	3.20	0.32	208	2096	3.39×10^5	9.33×10^4	2.34×10^5
4	3.22	0.36	121	1952	4.75×10^5	2.92×10^2	1.77×10^4
5	2.99	0.19	69	1787	9.88×10^4	1.12×10^4	1.07×10^5
6	3.18	0.24	121	1892	1.89×10^5	1.10×10^3	1.86×10^5
7	3.24	0.24	117	1788	2.07×10^5	3.53×10^4	1.57×10^5
8	3.04	0.33	118	2024	3.42×10^5	9.27×10^1	1.89×10^5
9	2.99	0.34	164	2063	3.42×10^5	6.61×10^2	2.77×10^5
10	2.99	0.35	171	2072	3.56×10^5	8.13×10^2	7.14×10^5
11	2.94	0.37	183	2091	3.73×10^5	1.14×10^4	2.70×10^5
12	2.81	0.33	81	1982	3.27×10^5	5.49×10^2	2.40×10^5
13	3.00	0.31	81	2203	2.77×10^5	7.80×10^2	2.40×10^5
14	2.86	0.08	54	2572	1.42×10^4	8.07×10^4	3.00×10^4
15	2.86	0.08	54	2585	1.42×10^4	2.85×10^4	8.00×10^4
16	2.78	0.08	49	3185	1.17×10^4	1.48×10^4	1.00×10^5

[a] Experimental results of **1–7** are from ref. 21 in CH_2Cl_2, of **8–11** are from ref. 22 in 2-MeTHF, of **12–13** are from ref. 23 in CH_2Cl_2, of **14–16** are from ref. 24 in CH_2Cl_2, respectively.

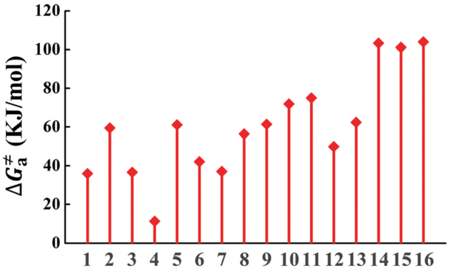

Fig. 3 Bar graph of the calculated Gibbs free energy ($\Delta G_a^{\neq}$) of activation energy between ^{3}ES and ^{3}TS.

The displacement vectors of the imaginary frequency in Fig. S6 (ESI†) are all rotational vibrations of the pyridine ring in the **L1** part, indicating the rationality of these ^{3}TS states. In addition, the displacement vectors of the imaginary frequency in ^{3}TS' states for complexes **1**, and **8–12** exhibited in Fig. S7 (ESI†) also indicate the reasonability of these ^{3}TS' states.

Table 4 Calculated rates (k_a) between ^{3}ES and ^{3}TS states, values of k_{nr}^{MC} beyond the harmonic region, and calculated phosphorescent quantum yields without considerations of k_{nr}^{MC} (Φ_p^{TVCF}) and with considerations of k_{nr}^{MC} (Φ_p^{MC}), as well as experimental measurements Φ_p (exp.)

	k_a (s^{-1},cal.)	$k_{nr}^{MC\,a}$ (s^{-1},cal.)	Φ_p^{TVCF} %	Φ_p^{MC} %	$\Phi_p^{\,b}$ (exp.) %
1	3.15×10^6	1.95×10^4	98.78	93.11	71.00
2	2.41×10^2	—	90.57	90.57	89.00
3	2.39×10^6	3.83×10^{-11}	78.44	78.44	82.00
4	6.70×10^{10}	8.06×10^5	99.94	37.05	45.00
5	1.22×10^2	—	89.81	89.81	95.00
6	2.63×10^5	1.10×10^3	99.42	98.29	78.00
7	2.99×10^6	3.05×10^{-3}	85.45	85.45	85.00
8	8.24×10^2	—	99.97	99.97	100.00
9	1.12×10^2	—	99.81	99.81	100.00
10	1.55×10^0	—	99.77	99.77	100.00
11	4.51×10^{-1}	—	97.04	97.04	100.00
12	1.11×10^4	—	99.83	99.83	95.00
13	7.44×10^1	—	99.72	99.72	90.00
14	4.99×10^{-6}	—	14.95	14.95	34.00
15	1.20×10^{-5}	—	33.21	33.21	44.00
16	3.85×10^{-6}	—	44.20	44.20	33.00

[a] "—" means there is no need to consider k_{nr}^{MC} due to the small k_a. [b] Experimental results of **1–7** are from ref. 21 in CH_2Cl_2, of **8–11** are from ref. 22 in 2-MeTHF, of **12** and **13** are from ref. 23 in CH_2Cl_2, of **14–16** are from ref. 24 in CH_2Cl_2, respectively.

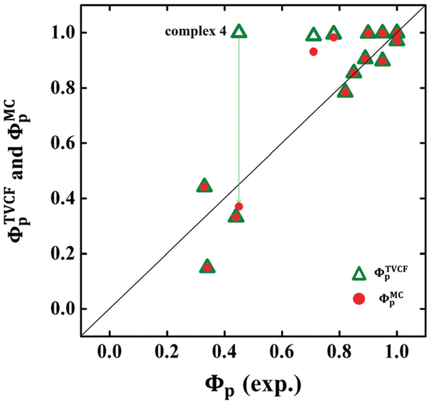

Fig. 4 Comparison between calculated Φ_p^{TVCF} (green hollow triangle) or Φ_p^{MC} (red solid circle) and experimental Φ_p (exp.) for 16 Pt(II) complexes.

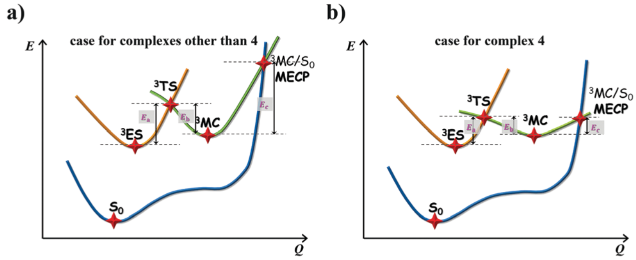

Fig. 5 Schematic representation of the competing excited-state deactivations of (a) complexes other than **4** that either ^{3}TS is high or MECP is unreachable; (b) complex **4** that both ^{3}TS and MECP are low in energy.

The calculated Gibbs free energies ($\Delta G_a^{\neq}$) for these Pt(II) complexes are listed in Table S3 (ESI†), and the bar graph depicted in Fig. 3 shows that complex **4** (*i.e.*, **PtON1-oMe**) has the lowest val. According to eqn ((5) and (6)), k_a and k_{nr}^{MC} can be quantitatively calculated, and the results are listed in Table 4. Complexes except for **1**, **3**, **4**, **6** and **7** have k_a of not more than 10^4 s^{-1}, which are uncompetitive with their k_r and k_{nr}^{TVCF}; therefore, deactivations *via* ^{3}TS and MECP can be ignored (k_a' was also uncompetitive with k_r and k_{nr}^{TVCF} for **8–12**, as given in Table S4, ESI†). Although k_a' (2.85×10^6 s^{-1}) for complex **1** was comparable to its k_a (3.15×10^6 s^{-1}), the MECP' was so high in energy ($E_c = 1.21$ eV, as listed in Table S5, ESI†) that the calculated k_{nr}^{MC} was only $\sim 10^{-14}$ s^{-1}. Hence, the non-radiative decay *via* this channel not need be considered. As for **1**, **3**, **4**, **6** and **7**, the structures of MECP were optimized by increasing the torsion angle of the **L1** part, as shown in Fig. S8 (ESI†). Comparing calculated Φ_p^{TVCF} andΦ_p^{MC} with experimental measurements of Φ_p (exp.), as shown in Fig. 4, Φ_p^{TVCF} was in accordance with Φ_p (exp.) for the majority of these blue-emitting tetradentate Pt(II) complexes owing to either their high ^{3}TS or unreachable MECP, deactivations *via* direct vibrational relaxation were dominant (see schematic case in Fig. 5a). Only for complex **4**, whereby both ^{3}TS and MECP are low in energy (as the schematic case shown in Fig. 5b), the deactivations beyond the harmonic region must be taken into account. Therefore, the TVCF framework was fairly accurate in the Φ_p predictions for most of these blue-emitting tetradentate Pt(II) complexes.

Conclusion

In summary, this study presents a computational scheme to evaluate the phosphorescence quantum efficiency by considering all possible triplet deactivation rates. It was applied to 16 blue-emitting tetradentate Pt(II) complexes characterized recently in experiments. Although all these Pt(II) complexes contained fused 5/6/6 metallocycles, their monomeric photophysical properties are dissimilar. Within the harmonic deactivation region, their ^{3}ES → S$_0$ transitions are ^{3}LLCT or ^{3}IL mixed with ^{3}MLCT characters. The calculated k_r of these complexes are in the range of 10^4 s^{-1}–10^5 s^{-1}, which is consistent with experiments, and the computed non-radiative decay rates within the harmonic region (k_{nr}^{TVCF}) are less than 10^5 s^{-1}. By going beyond the harmonic deactivation region, the structures of ^{3}TS and ^{3}MC are optimized for all complexes, and non-radiative decay rates k_{nr}^{MC} are quantitatively calculated. It is noteworthy that for the majority of these tetradentate Pt(II) complexes, the phosphorescence quantum efficiencies within the harmonic region Φ_p^{TVCF} are in well accordance with experimental observations. Only for **PtON1-oMe**, with both ^{3}TS and MECP low in energy, considering k_{nr}^{MC} is necessary. Given the accuracy of the TVCF framework, potential valuable blue-emitting tetradentate Pt(II) complexes can be designed and screened out efficiently.

Conflicts of interest

There are no conflicts of interest to declare.

Acknowledgements

This work is dedicated to Prof. Seth Marder, a brilliant mind in organic electronic materials chemistry, for his 60th birthday. ZS has been inspired by Seth's sharp mind and persistence in pursuit of science. This work is supported by the National Natural Science Foundation of China (Grant No. 21788102 and 21973099), the Ministry of Science and Technology of China (Grant No. 2017YFA0204501) and the Strategic Priority Research Program of the Chinese Academy of Sciences (Grant No. XDB12020200).

Notes and references

1 C. Adachi, M. A. Baldo, M. E. Thompson and S. R. Forrest, *J. Appl. Phys.*, 2001, **90**, 5048–5051.
2 Y. Chi and P.-T. Chou, *Chem. Soc. Rev.*, 2010, **39**, 638–655.
3 V. W.-W. Yam, V. K.-M. Au and S. Y.-L. Leung, *Chem. Rev.*, 2015, **115**, 7589–7728.
4 I. Omae, *Coord. Chem. Rev.*, 2016, **310**, 154–169.
5 T. Fleetham, G. Li and J. Li, *Adv. Mater.*, 2017, **29**, 1601861.
6 M. Mao, T.-L. Lam, W.-P. To, X. Lao, W. Liu, S. Xu, G. Cheng and C.-M. Che, *Adv. Mater.*, 2021, **33**, 2004873.
7 W.-S. Tai, L.-Y. Hsu, W.-Y. Hung, Y.-Y. Chen, C.-L. Ko, X. Zhou, Y. Yuan, A. K.-Y. Jen and Y. Chi, *J. Mater. Chem. C*, 2020, **8**, 13590–13602.
8 T. Fleetham, G. Li, L. Wen and J. Li, *Adv. Mater.*, 2014, **26**, 7116–7121.
9 X.-C. Hang, T. Fleetham, E. Turner, J. Brooks and J. Li, *Angew. Chem., Int. Ed.*, 2013, **52**, 6753–6756.
10 K. Li, Q. Wan, C. Yang, X.-Y. Chang, K.-H. Low and C.-M. Che, *Angew. Chem., Int. Ed.*, 2018, **57**, 14129–14133.
11 K. Li, G. S. Ming Tong, Q. Wan, G. Cheng, W.-Y. Tong, W.-H. Ang, W.-L. Kwong and C.-M. Che, *Chem. Sci.*, 2016, **7**, 1653–1673.
12 W.-C. Chen, C. Sukpattanacharoen, W.-H. Chan, C.-C. Huang, H.-F. Hsu, D. Shen, W.-Y. Hung, N. Kungwan, D. Escudero, C.-S. Lee and Y. Chi, *Adv. Funct. Mater.*, 2020, **30**, 2002494.
13 S. K. Fung, T. Zou, B. Cao, T. Chen, W.-P. To, C. Yang, C.-N. Lok and C.-M. Che, *Nat. Commun.*, 2016, **7**, 10655.
14 G. Cheng, Y. Kwak, W.-P. To, T.-L. Lam, G. S. M. Tong, M.-K. Sit, S. Gong, B. Choi, W. Il Choi, C. Yang and C.-M. Che, *ACS Appl. Mater. Interfaces*, 2019, **11**, 45161–45170.
15 A. Heil and C. M. Marian, *Inorg. Chem.*, 2019, **58**, 6123–6136.
16 W. H. Lam, E. S.-H. Lam and V. W.-W. Yam, *J. Am. Chem. Soc.*, 2013, **135**, 15135–15143.
17 A. Osipov, I. Kim, A. Odinokov, W.-J. Son, A. Yakubovich and H. Choi, *J. Phys. Chem. C*, 2020, **124**, 12039–12048.
18 X. Wang, T. Peng, C. Nguyen, Z.-H. Lu, N. Wang, W. Wu, Q. Li and S. Wang, *Adv. Funct. Mater.*, 2017, **27**, 1604318.
19 W. Zhang, J. Ma, G.-J. Liu, X.-Y. Liu, J. Fan and L.-S. Liao, *J. Mater. Chem. C*, 2017, **5**, 9496–9503.
20 Y. Wu, X. Tan, A. Lv, F. Yu, H. Ma, K. Shen, Z. Sun, F. Chen, Z.-K. Chen and X.-C. Hang, *J. Phys. Chem. Lett.*, 2019, **10**, 5105–5110.
21 G. Li, A. Wolfe, J. Brooks, Z.-Q. Zhu and J. Li, *Inorg. Chem.*, 2017, **56**, 8244–8256.
22 G. Li, X. Zhao, T. Fleetham, Q. Chen, F. Zhan, J. Zheng, Y.-F. Yang, W. Lou, Y. Yang, K. Fang, Z. Shao, Q. Zhang and Y. She, *Chem. Mater.*, 2020, **32**, 537–548.
23 L. Zhu, W. Xie, C. Qian, W. Xie, K. Shen, A. Lv, H. Ma, H. Li, X.-C. Hang, W. Li, S.-J. Su and W. Huang, *Adv. Opt. Mater.*, 2020, **8**, 2000406.
24 F. Yu, Y. Sheng, D. Wu, K. Qin, H. Li, G. Xie, Q. Xue, Z. Sun, Z. Lu, H. Ma and X.-C. Hang, *Inorg. Chem.*, 2020, **59**, 14493–14500.
25 Q. Peng, Y. Yi, Z. Shuai and J. Shao, *J. Am. Chem. Soc.*, 2007, **129**, 9333–9339.
26 Q. Peng, Y. Niu, Q. Shi, X. Gao and Z. Shuai, *J. Chem. Theory Comput.*, 2013, **9**, 1132–1143.
27 Q. Peng, Q. Shi, Y. Niu, Y. Yi, S. Sun, W. Li and Z. Shuai, *J. Mater. Chem. C*, 2016, **4**, 6829–6838.
28 Z. Shuai, *Chin. J. Chem.*, 2020, **38**, 1223–1232.
29 X. Zhang, D. Jacquemin, Q. Peng, Z. Shuai and D. Escudero, *J. Phys. Chem. C*, 2018, **122**, 6340–6347.
30 D. Escudero, *Chem. Sci.*, 2016, **7**, 1262–1267.
31 Y. Niu, W. Li, Q. Peng, H. Geng, Y. Yi, L. Wang, G. Nan, D. Wang and Z. Shuai, *Mol. Phys.*, 2018, **116**, 1078–1090.
32 Y. Niu, Q. Peng, C. Deng, X. Gao and Z. Shuai, *J. Phys. Chem. A*, 2010, **114**, 7817–7831.
33 H. Eyring, *J. Chem. Phys.*, 1935, **3**, 107–115.
34 T. Lu and Q. Chen, *Comput. Theor. Chem.*, 2021, **1200**, DOI: 10.1016/j.comptc.2021.113249.
35 M. J. Frisch, G. W. Trucks, H. B. Schlegel, G. E. Scuseria, M. A. Robb, J. R. Cheeseman, G. Scalmani, V. Barone, G. A. Petersson, H. Nakatsuji, X. Li, M. Caricato, A. V. Marenich, J. Bloino, B. G. Janesko, R. Gomperts, B. Mennucci, H. P. Hratchian, J. V. Ortiz, A. F. Izmaylov, J. L. Sonnenberg, D. Williams-Young, F. Ding, F. Lipparini, F. Egidi, J. Goings, B. Peng, A. Petrone, T. Henderson, D. Ranasinghe, V. G. Zakrzewski, J. Gao, N. Rega,

G. Zheng, W. Liang, M. Hada, M. Ehara, K. Toyota, R. Fukuda, J. Hasegawa, M. Ishida, T. Nakajima, Y. Honda, O. Kitao, H. Nakai, T. Vreven, K. Throssell, J. A. Montgomery Jr., J. E. Peralta, F. Ogliaro, M. J. Bearpark, J. J. Heyd, E. N. Brothers, K. N. Kudin, V. N. Staroverov, T. A. Keith, R. Kobayashi, J. Normand, K. Raghavachari, A. P. Rendell, J. C. Burant, S. S. Iyengar, J. Tomasi, M. Cossi, J. M. Millam, M. Klene, C. Adamo, R. Cammi, J. W. Ochterski, R. L. Martin, K. Morokuma, O. Farkas, J. B. Foresman and D. J. Fox, *Gaussian 16, Revision A.01*, Gaussian, Inc., Wallingford CT, 2016.

36 J. P. Perdew, K. Burke and M. Ernzerhof, *Phys. Rev. Lett.*, 1996, **77**, 3865–3868.

37 S. Grimme, J. Antony, S. Ehrlich and H. Krieg, *J. Chem. Phys.*, 2010, **132**, 154104.

38 A. D. Becke and E. R. Johnson, *J. Chem. Phys.*, 2005, **123**, 154101.

39 T. Lu, *sobMECP program*, 2020, http://sobereva.com/286.

40 J. Tomasi, B. Mennucci and R. Cammi, *Chem. Rev.*, 2005, **105**, 2999–3094.

41 D. Andrae, U. Häußermann, M. Dolg, H. Stoll and H. Preuß, *Theor. Chim. Acta*, 1990, **77**, 123–141.

42 Y. Zhao and D. G. Truhlar, *Theor. Chem. Acc.*, 2008, **120**, 215–241.

43 X. Gao, S. Bai, D. Fazzi, T. Niehaus, M. Barbatti and W. Thiel, *J. Chem. Theory Comput.*, 2017, **13**, 515–524.

44 K. Aidas, C. Angeli, K. L. Bak, V. Bakken, R. Bast, L. Boman, O. Christiansen, R. Cimiraglia, S. Coriani, P. Dahle, E. K. Dalskov, U. Ekström, T. Enevoldsen, J. J. Eriksen, P. Ettenhuber, B. Fernández, L. Ferrighi, H. Fliegl, L. Frediani, K. Hald, A. Halkier, C. Hättig, H. Heiberg, T. Helgaker, A. C. Hennum, H. Hettema, E. Hjertenæs, S. Høst, I.-M. Høyvik, M. F. Iozzi, B. Jansík, H. J. A. Jensen, D. Jonsson, P. Jørgensen, J. Kauczor, S. Kirpekar, T. Kjærgaard, W. Klopper, S. Knecht, R. Kobayashi, H. Koch, J. Kongsted, A. Krapp, K. Kristensen, A. Ligabue, O. B. Lutnæs, J. I. Melo, K. V. Mikkelsen, R. H. Myhre, C. Neiss, C. B. Nielsen, P. Norman, J. Olsen, J. M. H. Olsen, A. Osted, M. J. Packer, F. Pawlowski, T. B. Pedersen, P. F. Provasi, S. Reine, Z. Rinkevicius, T. A. Ruden, K. Ruud, V. V. Rybkin, P. Sałek, C. C. M. Samson, A. S. de Merás, T. Saue, S. P. A. Sauer, B. Schimmelpfennig, K. Sneskov, A. H. Steindal, K. O. Sylvester-Hvid, P. R. Taylor, A. M. Teale, E. I. Tellgren, D. P. Tew, A. J. Thorvaldsen, L. Thøgersen, O. Vahtras, M. A. Watson, D. J. D. Wilson, M. Ziolkowski and H. Ågren, *Wiley Interdiscip. Rev.: Comput. Mol. Sci.*, 2014, **4**, 269–284.

45 *Dalton, a molecular electronic structure program, Release v2017.alpha*, 2017, http://daltonprogram.org.

46 A. D. Becke, *J. Chem. Phys.*, 1993, **98**, 5648–5652.

47 C. Lee, W. Yang and R. G. Parr, *Phys. Rev. B: Condens. Matter Mater. Phys.*, 1988, **37**, 785–789.

48 T. Lu and F. Chen, *J. Comput. Chem.*, 2012, **33**, 580–592.

49 Z. Liu, T. Lu and Q. Chen, *Carbon*, 2020, **165**, 461–467.

50 G. S. M. Tong, P. K. Chow, W. P. To, W. M. Kwok and C. M. Che, *Chem. – Eur. J.*, 2014, 6433–6443.

51 Q. Ou and J. E. Subotnik, *J. Phys. Chem. C*, 2013, **117**, 19839–19849.

52 S. Arroliga-Rocha and D. Escudero, *Inorg. Chem.*, 2018, **57**, 12106–12112.